

IoT-Enabled Coordinated Virtual Synchronous Generator Inertia Optimization Strategy for Flexible Interconnected Distribution Networks

Lei Su^{1,2,3}, Mingjiang Wei^{1,2,3}, Junda Qin^{4,*}, Runfa Wu⁴, Kan Cao^{1,2,3}, Ziya Chen^{1,2,3}

¹State Grid Hubei Electric Power Research Institute, Wuhan 430077, Hubei, China

²Hubei Key Laboratory of Regional New Power Systems and Rural Energy System Configuration, Wuhan 430077, Hubei, China

³Hubei Engineering Research Center of the Construction and Operation Control Technology of New Power Systems, Wuhan 430077, Hubei, China

⁴State Key Laboratory of Advanced Power Transmission Technology (China Electric Power Research Institute Co., Ltd.), Beijing 100192, China

Received 15 Sep 2025

Accepted 12 Feb 2026

Abstract

The integration of renewable energy sources (RES) into flexible interconnected distribution networks (FIDNs) has reduction in system equivalent inertia, posing a severe threat to frequency stability and dynamic response capability. To address this challenge, this paper proposes a dynamic coordinated inertia optimization strategy for Virtual Synchronous Generators (VSGs), leveraging coordination among Internet-of-Things (IoT) devices. Initially, an IoT sensing architecture is constructed to enable synchronized acquisition of operational data from distributed generators (DGs), flexible loads, and energy storage systems. An online inertia demand prediction model, driven by multi-source heterogeneous data fusion, is established. This model facilitates the perception and quantitative analysis of inertia demand variations across different network regions and operating conditions. Subsequently, by integrating VSG small-signal stability constraints, an adaptive inertia parameter optimization algorithm is designed. This algorithm achieves the coordinated and fine-tuned adjustment of critical VSG parameters—such as virtual inertia and damping coefficients—thereby significantly enhancing the system's frequency disturbance rejection capability and recovery resilience. The efficacy of the proposed IoT-enabled coordinated optimization framework is validated through a Hardware-in-the-Loop (HIL) simulation testbed. Simulation results demonstrate that the proposed strategy effectively suppresses frequency fluctuation magnitudes and achieves rapid recovery within 100 milliseconds, markedly improving the system's transient stability and fault ride-through capability. This research provides an IoT-enabled coordinated optimization solution to the challenge of inertia support in distribution networks under high-penetration renewable energy integration, offering robust technical support for the secure and stable operation of new power systems.

© 2026 Jordan Journal of Mechanical and Industrial Engineering. All rights reserved

Keywords: Flexible interconnected distribution network (FIDN), Internet of Things (IoT), Virtual synchronous generator (VSG), Hardware-in-the-loop (HIL) testing, Control strategy, Automatic optimization.

1. Introduction

Large-scale integration of high-penetration renewable energy sources (RES)—such as wind and photovoltaic generation—into distribution networks has led to a steady decline in system equivalent rotational inertia. Replacing conventional synchronous generators with inverter-interfaced units directly impairs system frequency response characteristics [1-2]. This manifests as a significant rise in the Rate of Change of Frequency (RoCoF), deeper frequency nadirs, and reduced dynamic stability margins during load fluctuations or fault disturbances. Statistics show that in regional distribution networks with over 30% renewable energy penetration, equivalent inertia usually drops by 40%–60%, severely restricting the grid's disturbance resilience. This has become a key challenge for power systems with high-penetration RES [3-5]. Flexible

Interconnected Distribution Networks (FIDNs)—which use power electronic converters for topology reconfiguration and flexible power dispatching—provide a promising approach to inertia enhancement. Their technical foundation relies on multi-terminal interconnected architecture, virtual inertia emulation, and distributed coordinated control [6-7]. A multi-terminal interconnected structure is developed in [8-9], which uses flexible switches to form a meshed network topology and overcome power flow regulation constraints in conventional radial distribution systems. In [10-11], virtual inertia emulation techniques are proposed, where Virtual Synchronous Generator (VSG) control strategies endow power converters with synchronous machine-like external characteristics and support active inertia responses. Building on this foundation, distributed coordinated control frameworks are proposed in [12-13] to integrate distributed energy resources (DERs)—including energy storage

* Corresponding author e-mail: 17896002462@163.com.

systems and controllable loads—into a unified "virtual inertia reserve". Empirical results indicate FIDNs can double or even triple the system's equivalent inertia. This improvement largely depends on developing a coordinated optimization model covering generation, network, load, and storage (G-N-L-S) components, which dynamically matches inertia resources across time and space [14]. However, current research on FIDNs mostly focuses on single-converter VSG control strategies—including damping ratio optimization and adaptive virtual inertia algorithms—or stability analysis in simple parallel systems. Multi-converter coordinated control still faces key challenges: First, discrepancies in local measurements among adjacent VSG units lead to counter-phase superposition of virtual torques; Second, conventional centralized optimization frameworks struggle to achieve real-time coordination of decentralized parameters; Third, stability constraints are often overlooked—most studies fail to include small-signal stability boundaries, which can trigger sub-synchronous oscillations (SSO). These issues ultimately result in suboptimal inertia support performance in real-world engineering applications. Internet of Things (IoT) technologies provide a new way to tackle the aforementioned challenges [15]. First, 5G communication has latency under 10 ms, enabling accurate system-wide data synchronization [16-17]. Meanwhile, coordinated control frameworks have advanced significantly, with standardized device interoperability architectures (e.g., IEEE P2668) enabling "plug-and-play" collaboration between power converters from different manufacturers [18-19]. Additionally, edge computing and related technologies support distributed reinforcement learning algorithms, allowing millisecond-timescale coordinated inertia decision-making [20]. Together, these developments make it possible to create FIDNs with close integration of IoT devices and power converters, resolving the core problem of multi-agent control mismatch. This paper proposes a three-tier architecture consisting of "IoT-enabled Perception," "Coordinated Prediction," and "Dynamic Optimization." In the IoT Perception Tier, a reliable, ultra-low-latency IoT sensing infrastructure is designed to collect real-time, high-precision operational data from distributed generation (DG) units, flexible loads, and energy storage systems. Based on this data foundation, an online inertia demand prediction model using multi-source heterogeneous data fusion is established. This model supports accurate identification and quantitative analysis of changes in system inertia requirements under different operating conditions. Next, by fully integrating VSG small-signal stability constraints, an adaptive inertia parameter optimization algorithm is developed. This algorithm dynamically and coordinately adjusts key VSG parameters—including virtual inertia and damping coefficients—with fine-grained control, markedly enhancing the system's frequency disturbance rejection and recovery capabilities.

2. SMART DISTRIBUTION NETWORK PLATFORM BASED ON IOT ARCHITECTURE

Addressing the challenge of dynamic inertia perception induced by high-penetration renewable energy integration, this chapter constructs an IoT-enabled smart distribution network platform founded upon Cloud-Edge-Terminal collaboration (Figure 1). The Cloud Intelligence Tier, deployed via a Platform-as-a-Service (PaaS) architecture, provides million-scale message processing capability

(>10⁶ messages per second) alongside containerized application hosting. The Edge Tier, leveraging ARMv8-based platforms, implements graphical programming conforming to the IEC 61499 standard, enabling remote batch deployment of terminal software within 50 milliseconds. The Station/Field Tier employs a hierarchical distributed structure interconnected via a dual-redundant fiber-optic ring network (exhibiting propagation latency $\leq 2 \mu\text{s}$). Through a hierarchical communication mechanism (Platform Tier $\leq 100 \text{ ms}$, Station Control Tier $\leq 4 \mu\text{s}$, I/O Tier $\leq 100 \mu\text{s}$) and a triplicated reliability design (comprising dual-redundant control + two-out-of-three (2oo3) protection + cross-interconnected bus), this architecture furnishes a highly reliable hardware foundation for real-time inertia perception and transmission, thereby underpinning the implementation of subsequent optimization control strategies.

2.1. IoT Collaborative Architecture

To address the requirement for dynamic inertia perception in distribution networks with high-penetration renewables, this chapter proposes the three-tier IoT collaborative architecture depicted in Figure 1. The primary tier constitutes the Cloud Intelligence Platform, deployed within a cloud-based Resource-Platform-Application (PaaS) framework, providing a distributed data engine (throughput $> 10^6 \text{ msg/s}$) and a containerized application hosting environment (Docker/Kubernetes). The secondary tier represents the Edge Visualization Programming Layer, based upon an ARMv8-architecture embedded development platform. This layer supports graphical logic configuration (adhering to the IEC 61499 standard), facilitating remote batch deployment of terminal device software (achieving OTA upgrade latency $< 50 \text{ ms}$). The tertiary tier encompasses the Station-level Control Layer, employing a hierarchical distributed structure (illustrated in Figure 2). This layer interconnects the cloud platform and local devices via a dual-redundant fiber-optic ring network (characterized by transmission latency $\leq 2 \mu\text{s}$), thereby establishing a closed-loop collaborative perception system spanning Cloud-Edge-Terminal.

2.2. Design of High-Reliability Communication Mechanism

The real-time performance and reliability of the IoT collaborative architecture are critically contingent upon the precise adaptation of hierarchical communication channels. To satisfy the disparate requirements inherent in "cloud decision-making – station control execution – local acquisition," a strictly graded communication service hierarchy must be established. Table 1 quantitatively defines the key parameters for each communication layer, providing the requisite constraint boundaries for the subsequent eTDM bus design.

Table 1. Key Real-Time Requirements for Each Communication Layer

Tier	Communication Medium	Real-Time Performance Metric
Platform Control Tier	Power Data Network / Dedicated Line	Latency $\leq 100 \text{ ms}$
Station Control Tier	Dual-Redundant LAN Fiber Optics	Latency $\leq 4 \mu\text{s}$
I/O Device Tier	eTDM Bus	Cycle Time $\leq 100 \mu\text{s}$

2.3. eTDM High-Speed Bus Technology

To fulfill the stringent real-time requirements for inertia perception (mandating a sampling period $\leq 100 \mu s$), an eTDM bus featuring reconfigurable frame structure is engineered. The eTDM bus employs a dual-mode communication mechanism. In source-synchronous mode, clock signals are transmitted in parallel with data (link count $\times 2$), supporting 100 Mbps transmission rates (exhibiting a bit error rate $< 10^{-12}$). Conversely, in asynchronous mode, single-link transmission is utilized, rendering it suitable for low-bandwidth scenarios.

2.4. Multiplexed Reliability Assurance Design

To guarantee long-term operational reliability, a triplex protection mechanism is architected: (I) Triple-Modular

Control & Protection: The DC control system adopts a physically isolated dual-redundant architecture (independent A/B systems with segregated power supplies, acquisition cards, and eTDM buses). Protection equipment incorporates two-out-of-three (2oo3) voting logic (ensuring spurious operation probability $< 10^{-9}$). (II) Redundant Signal Acquisition: Analog inputs: Utilize dual independent CT/VT windings \rightarrow dual-channel AD conversion (maintaining error $< \pm 0.1\%$). Digital inputs: Employ dual-node acquisition \rightarrow optoelectronic isolation \rightarrow dual-bus transmission. (III) Fault-Tolerant Network Topology: Station control layer: Implements a self-healing ring network architecture. eTDM bus: Operates in cross-interconnection mode (Figure 2).

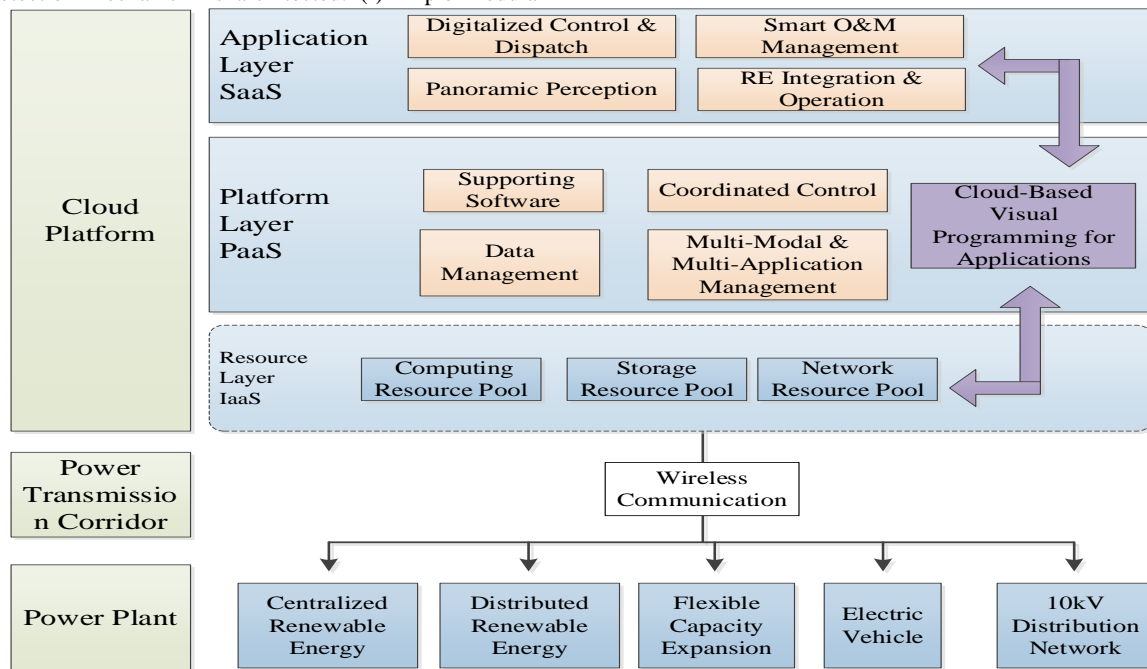


Figure 1. Architecture of the IoT collaborative smart distribution network platform

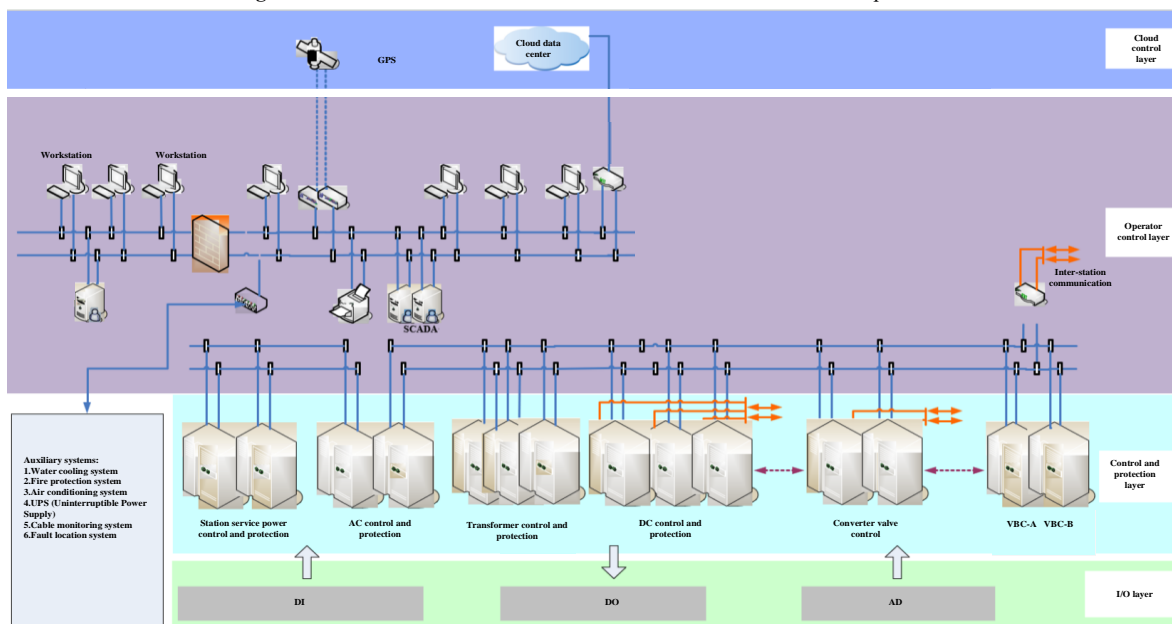


Figure 2. Schematic diagram of the station-level overall architecture

3. VIRTUAL SYNCHRONOUS GENERATOR INERTIA CHARACTERISTICS AND DEMAND PERCEPTION

This chapter delineates the inertia support mechanism of Virtual Synchronous Generators (VSGs) and quantifies its operational constraints. Initially, the intrinsic "zero physical inertia" characteristic of VSGs is analytically deconstructed, wherein an innovative speed regulation coefficient (λ) is introduced. It is rigorously demonstrated that for $\lambda > 1$, the equivalent inertia can be augmented up to threefold its nominal value, thereby surmounting the inherent inertia deficiency bottleneck in renewable energy installations. Subsequently, an adaptive inertia control framework is formulated—delimiting stability boundaries via small-signal modeling and incorporating a threshold-triggered algorithm to dynamically modulate the inertia parameter J . This approach resolves the inherent dilemma between transient overshoot and steady-state oscillation prevalent in fixed-inertia schemes. Conclusively, investigations employing a single-station infinite-bus system elucidate the inertia-damping coupling phenomenon: Diminishing electrical distance ($X \downarrow \rightarrow Kd \uparrow$) enhances damping capability. Conversely, system expansion beyond a critical threshold ($S/Sh > 1.0$) precipitates a 65% deterioration in damping. These empirical findings furnish pivotal design constraints for advanced control strategies.

3.1. Analysis of Virtual Synchronous Generator Inertia Characteristics

The pervasive integration of high-penetration renewable energy induces substantial attenuation in grid equivalent inertia, thereby critically jeopardizing system frequency stability. Fundamentally, while Virtual Synchronous Generators (VSGs), governed by power electronic converters, possess flexible power regulation capabilities, they inherently lack the autonomous frequency transient suppression mechanism afforded by the rotational kinetic energy of conventional synchronous generators. To address this fundamental limitation, an in-depth analytical deconstruction of VSG inertia characteristics is conducted: (i) The VSG rotor motion equation is formulated, elucidating the mechanism whereby frequency deviations trigger dynamic active power responses, thereby emulating the inertial behavior of synchronous machines. (ii) An innovative speed regulation coefficient (λ) is introduced. It is rigorously proven that for $\lambda > 1$, VSGs transcend inherent physical inertia constraints, delivering equivalent virtual inertia multiple times their nominal value over extended speed ranges. This intrinsic characteristic establishes the theoretical foundation for the subsequent adaptive inertia control strategy design, ultimately enabling renewable energy installations to undergo a functional paradigm shift from "inertia deficiency" to "active support".

3.1.1. Inertia Deficiency Mechanism and Virtual Inertia

Unlike conventional synchronous generators, VSG converter stations controlled via power electronic converters are intrinsically incapable of autonomous inertial support. However, they exhibit highly flexible and controllable active power regulation. Consequently, VSG-based converter clusters not only emulate inertial response through rapid active power adjustments—modulating virtual rotor speed to release or absorb rotational kinetic energy—but also synthesize virtual inertia exceeding their inherent

physical inertia magnitude across broader speed regulation ranges.

For a conventional synchronous generator unit, neglecting damping effects, the rotational kinetic energy (E_k) stored within its mechanical rotor component is expressed as:

$$E_k = \int (PG_m - PG) = \int J_s \omega_m d\omega_m = \frac{1}{2} J_s \omega_m^2 = \frac{1}{2p_s} J_s \omega_c^2 \quad (1)$$

In Eq. (1), ω_m and ω_c denote the generator's mechanical angular velocity and synchronous electrical angular velocity, respectively; J_s and p_s represent the moment of inertia and number of pole pairs, respectively; PG_m and PG signify the mechanical power input and electromagnetic power output, respectively. Within the domain of power system analysis, the inertia time constant H_s is conventionally defined as the ratio of the rotational kinetic energy stored in the generator rotor operating at synchronous angular velocity ω_c to the machine's rated apparent power S_N , expressed mathematically as Eq. (2):

$$H_s = \frac{J_s \omega_c^2}{2p_s^2 S_N} \quad (2)$$

Building upon the definition of the inertia time constant given in (1), the equivalent system inertia time constant H for a power network integrated with Virtual Synchronous Generator (VSG) converter stations can be derived as Eq. (3):

$$H = \frac{\sum_{i=1}^{i=n} \left(\frac{1}{2p_{si}^2} J_{si} \omega_e^2 \right) + \sum_{j=1}^{j=m} E_{kwj}}{S_N} \quad (3)$$

Where, n and m denote the number of synchronous generator units and variable-speed generator units within the system, respectively; J_{si} , p_{si} represent the moment of inertia and number of pole pairs of the i -th synchronous generator, respectively; S_N is the aggregate rated apparent power of the system; E_{kwj} signifies the rotational kinetic energy of the j -th Virtual Synchronous Generator unit.

As evidenced by the preceding analysis, Virtual Synchronous Generator (VSG) units cannot release or absorb rotor kinetic energy during grid frequency variations—a capability intrinsic to synchronous generators—as mathematically expressed Eq. (4):

$$\sum_{j=1}^m E_{kwj} \approx 0 \quad (4)$$

Consequently, the substitution of conventional converter stations with VSG-equipped stations diminishes the grid's utilizable kinetic energy reservoir without altering total power transmission, thereby reducing effective system inertia. Moreover, even under constant aggregate power transfer, the integration of Voltage-Source Converter (VSC)-HVDC stations—providing negligible kinetic energy contribution—coincident with capacity expansion further degrades effective system inertia. Thus, HVDC converter station integration inevitably diminishes effective system inertia, consequently jeopardizing frequency stability.

3.1.2. Inertia-Frequency Dynamic Response Model

We now analytically derive the equivalent virtual inertia synthesized by VSG converter stations through speed

regulation during frequency transients. The swing equation governing VSG converter dynamics is formulated as Eq. (5):

$$P_m - P_s = J_w \omega_r \frac{d\omega_r}{p_w^2 dt} \quad (5)$$

Where, P_m and P_s denote the mechanical power input and electromagnetic power output of the Virtual Synchronous Generator, respectively; p_w and J_w represent the number of pole pairs and inherent moment of inertia of the VSG unit, respectively.

Through active power regulation, Virtual Synchronous Generators (VSGs) endow their power output with dynamic responsiveness to system frequency variations, thereby emulating the inertial response characteristics inherent in conventional synchronous generator units. As derived from Eq. (1), the utilizable rotational kinetic energy (E_{kw}) of a VSG unit during frequency transients can be mathematically represented as Eq. (6):

$$E_{kw} = \int (P_m - P_s) dt = \int \frac{J_w \omega_r d\omega_r}{\omega_s d\omega_s} \times \frac{\omega_s d\omega_s}{p_w^2 dt} dt \quad (6)$$

Upon incorporating system frequency deviation signals into the Virtual Synchronous Generator (VSG) converter control system, its rapid active power regulation synthesizes rotational inertia emulation. Assuming the VSG converter station maintains constant virtual inertia during frequency transients, its supplemental kinetic energy contribution to the system is quantifiable as Eq. (7):

$$E_{kw} = \frac{1}{2} J_{vir} \left(\frac{\omega_c}{p_w} \right)^2 \quad (7)$$

Pursuant to Eq. (2), the equivalent virtual inertia time constant H_{vir} for the VSG converter station is formally defined Eq. (8):

$$H_{vir} = \frac{J_{vir} \omega_c^2}{2 p_w^2 S_N} \quad (8)$$

VSG converter stations endowed with virtual inertia exhibit inertial response characteristics analogous to conventional synchronous generators, thereby providing supplemental inertia support to the power system. This mechanism effectively mitigates the inertia degradation phenomenon induced by Voltage-Source Converter High-Voltage Direct Current (VSC-HVDC) grid integration.

The foregoing analysis establishes that VSG converter stations, through speed regulation during grid frequency excursions, synthesize equivalent rotational inertia, consequently reinforcing grid inertia. To enable optimal control of the defined virtual inertia, the virtual inertia term in Eq. (6) is reformulated as:

$$J_{vir} = \frac{J_w \omega_r d\omega_r}{\omega_s d\omega_s} \approx \frac{\Delta\omega_r}{\Delta\omega_s} \cdot \frac{\omega_{r0}}{\omega_c} J_w = \lambda \frac{\omega_{r0}}{\omega_c} J_w \quad (9)$$

In this formulation, λ denotes the speed regulation coefficient, defined as $\lambda = \Delta\omega_r / \Delta\omega_s$.

Eq. (9) elucidates that the virtual inertia of a VSG converter station is contingent not only upon its inherent moment of inertia, but also on the angular velocity ω_{r0} preceding the system frequency deviation and the speed regulation coefficient λ . Diverging fundamentally from synchronous generators—where rotor speed couples rigidly with grid frequency—VSG units permit $\Delta\omega_r$ to substantially exceed $\Delta\omega_c$ (i.e., $\Delta\omega_r > \Delta\omega_c$). Consequently, during virtual

inertia emulation, VSG converter stations may configure λ in accordance with grid requirements, thereby synthesizing tailored inertial responses.

Under conditions of diminished system equivalent inertia, prescribing $\lambda > 1$ enables VSG converters to generate augmented equivalent inertia—exceeding their inherent inertia by orders of magnitude across extended speed regulation ranges—thereby delivering enhanced stabilization support to system frequency dynamics.

3.2. Adaptive Inertia Parameter Design Methodology

The inertia parameterization of Virtual Synchronous Generators (VSGs) directly governs dynamic response performance and stability. While structurally straightforward, fixed-inertia schemes entail a fundamental compromise between transient rapidity and steady-state damping requirements (illustrated in Figure 3). To resolve this dichotomy, this section advances a co-design framework integrating stability constraints with adaptive control: (i) First, quantitative relationships among inertia parameter J , damping coefficient, and oscillatory dynamics are established via small-signal modeling, thereby demarcating safe operational boundaries; (ii) Subsequently, a threshold-triggered adaptive inertia control law is innovatively devised, surmounting the performance ceiling of fixed-inertia approaches through real-time J -value modulation. This methodology significantly enhances system disturbance rejection capability while rigorously preserving small-signal stability.

3.2.1. Small-Signal Stability Constraints

Adapted from the small-signal modeling techniques for traditional synchronous generators, the VSG swing equation yields a small-signal stability analysis model depicted in Figure 4. Notably, the input-output power response characteristic of a VSG constitutes a canonical second-order transfer function Eq. (10)-(11):

$$G(s) = \frac{Pe(s)}{Pm(s)} = \frac{\omega_0 SE / J}{S^2 + (D_p / J)S + \omega_0 SE / J} \quad (10)$$

Where SE denotes the per-unit value of synchronizing power.

$$SE = \frac{\partial P}{\partial \delta} = \frac{E_s U}{S_n Z} \sin(\alpha - \delta) \quad (11)$$

Where E_s and δ_s represent the steady-state operating equilibrium points associated with the commanded active power P_{ref} and reactive power Q_{ref} . Given known filter inductance parameters and constant grid voltage magnitude U , the following analytical solution is derived Eq. (12):

$$\begin{cases} \delta_s = \alpha - \tan^{-1} \left(\frac{Q_{ref} + U^2 \sin \alpha}{P_{ref} + U^2 \cos \alpha / Z} \right) \\ E_s = \frac{Q_{ref} Z + U^2 \sin \alpha}{U \sin(\alpha - \delta_s)} \end{cases} \quad (12)$$

Evidently, under specified active and reactive power commands, SE constitutes a time-invariant constant. Consequently, the natural oscillatory angular frequency and damping coefficient for the second-order system delineated in Eq. (13) can be derived as:

$$\begin{cases} \omega_n = \sqrt{\omega_0 SE / J} \\ \zeta = 0.5 D_p \sqrt{I / (\omega_0 SE J)} \end{cases} \quad (13)$$

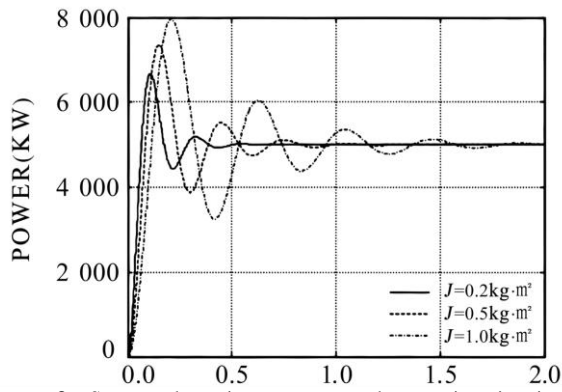


Figure 3. System dynamic response under varying inertia conditions

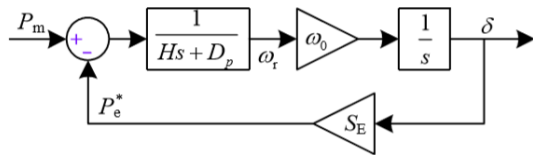


Figure 4. Small-Signal model of virtual synchronous generator converter station

3.2.2. Threshold-Triggered Adaptive Inertia Control

Conventional synchronous generators and fixed-virtual-inertia VSG-controlled inverters exhibit invariant natural oscillatory frequencies ω_n and damping ratios ξ . Consequently, VSG controller design typically emulates the natural oscillatory frequency range of synchronous generators (0.628–15.700 rad/s). Following determination of the VSG's oscillatory angular frequency, the requisite virtual inertia J is computed. Analogously, invoking the well-established optimal second-order system paradigm with $\zeta=0.707$, the desired damping coefficient D is derived from Eq. (13).

Quantitative analysis results under specified parameters ($L=1$ mH, $R=0.24$, $S_n=50$ kVA) demonstrate that at grid-connection active/reactive command values $P_{ref}=5$ kW and $Q_{ref}=0$ var, Eq. (12) yields the steady-state operating equilibrium point for power angle and electromotive force as $(\delta_s, E_s)=(0.0216\text{rad}, 382.45\text{V})$. Concomitantly, Eq. (11) computes $S_E=1.4593$.

Figure 4 illustrates the dynamic response characteristics of the Virtual Synchronous Generator (VSG) converter station under varying rotational inertia conditions, wherein D_p denotes the damping coefficient tuned in accordance with the optimal second-order system paradigm. To achieve enhanced transient response agility during prescribed power variations, an adaptive virtual rotor inertia control strategy is formulated, synthesizing insights from the inertia-power oscillation relationship established in the preceding section. This methodology dynamically modulates the virtual rotor inertia J based on the concurrent evaluation of: (i) The virtual rotor angular velocity derivative $d\omega/dt$, (ii) The angular velocity deviation $\omega - \omega_g$ between the virtual rotor and grid. The virtual rotor inertia assignment principle governing this control scheme is mathematically prescribed by Eq. (14):

$$J = \begin{cases} J_0 & \frac{d\omega}{dt} \leq C \\ J_0 + k \frac{|\omega - \omega_g|}{(\omega - \omega_g)dt} \frac{d\omega}{dt} & \frac{d\omega}{dt} > C \end{cases} \quad (14)$$

where k denotes a constant coefficient. The incorporation of threshold C in Eq. (14) serves to mitigate unnecessary inertia variations induced by minor measurement inaccuracies inherent in detection processes, thereby ensuring system stability during steady-state operation. The adaptive control algorithm proposed in Eq. (14) incorporates two pivotal control variables: J_0 and coefficient k . Subsequent small-signal stability analysis will establish the permissible operational ranges for J_0 and k . The active and reactive power outputs of the VSG converter station are mathematically expressed as Eq. (15):

$$\begin{aligned} P &= \frac{E_e U}{Z} \cos(\theta - \delta) - \frac{U^2}{Z} \cos \theta \\ Q &= \frac{E_e U}{Z} \sin(\theta - \delta) - \frac{U^2}{Z} \sin \theta \end{aligned} \quad (15)$$

where E_e denotes the root mean square (RMS) value of the internal line-to-line voltage within the Virtual Synchronous Generator (VSG) converter station; Z and θ represent the output filter impedance magnitude and impedance angle, respectively. Within the voltage and current control loops of the VSG converter station, an equivalent output impedance is integrated into the controller architecture. The discrepancy between the controller's output impedance and the physical inverter output impedance exerts negligible impact on control system stability. The output filter impedance magnitude Z and impedance angle θ for the VSG converter station are represented as Eq. (16):

$$\begin{cases} Z = \sqrt{(\omega L)^2 + R^2} \\ \theta = \arctan \frac{\omega L}{R} \end{cases} \quad (16)$$

where $\Delta\delta$ and $\Delta\omega$ denote the deviations of the power angle and rotor angular frequency from their nominal values, respectively.

The characteristic roots of the Virtual Synchronous Generator converter station are expressed as Eq. (17):

$$P_{1,2} = -\frac{D}{2J} \pm \sqrt{\left(\frac{D}{2J}\right)^2 - \frac{S_E}{J\omega_0}} \quad (17)$$

Rooted in control theory principles, a second-order system achieves stability exclusively when both characteristic roots reside within the left-half complex plane. Given that D persists as a positive quantity, ensuring non-negativity of the damping inertia J during adaptive variation constitutes a necessary stability preservation criterion. As stipulated by Eq. (14), under elevated $|d\omega/dt|$ conditions, the angular frequency deviation $(\omega - \omega_g)$ solely governs the algebraic sign of coefficient k . Assuming $k = -\kappa$ under such operational regimes (where $\kappa > 0$), the minimal achievable inertia J is expressible in the following form Eq. (18):

$$J_{min} = J_0 - k \frac{d\omega}{dt} \Big|_{\max} \quad (18)$$

Synthesizing the above analyses, the implementation of adaptive inertia J necessitates comprehensive consideration in selecting the steady-state inertia J_0 and coefficient k . Elevated k values facilitate responsive inertia modulation proportional to the virtual rotor angular velocity derivative ($d\omega/dt$), thereby effectively mitigating transient overshoot. However, excessively large k values will potentially trigger $J < 0$, compromising system stability. While augmented J_0 values accommodate higher k magnitudes, Eq. (11) reveals that excessive J diminishes the system damping coefficient ζ , inducing prolonged underdamped oscillations detrimental to dynamic performance. Consequently, parameter selection for J_0 and k must holistically address the competing requirements of transient overshoot suppression and adequate damping preservation, demanding a tailored selection strategy.

3.3. Inertia-Damping Coupling Influence Mechanism

The inertia support capability of Virtual Synchronous Generators (VSGs) exhibits intrinsic coupling with system damping characteristics, directly governing frequency stability. To delineate their interaction mechanisms, this section conducts quantitative analysis based on a single-station infinite-bus system model: (i) Mathematical interdependencies between inertia and damping (Eqs. (18)-(26)) are established, revealing an inverse correlation between electrical distance (external reactance X) and damping strength; (ii) A dual-directional impact of system capacity scaling (S/S_b) on damping is identified—capacity expansion enhances damping below the critical threshold ($S/S_b = 1.0$), but precipitates a 65% deterioration beyond this operational point. These findings impose critical design constraints for adaptive inertia control strategy formulation.

3.3.1. Influence of Electrical Distance on Damping

To elucidate core mechanisms while maintaining analytical tractability, damping characteristics are investigated within a single-station infinite-bus system configuration (Figure 5), where X denotes the equivalent reactance between the point of common coupling (PCC) and the infinite bus.

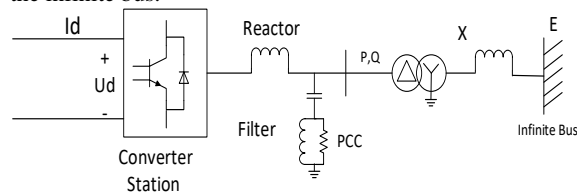


Figure 5. Single-Station Infinite-Bus System

Within this framework, the rotor dynamics equation for the Virtual Synchronous Generator converter station is formulated as Eq. (18):

$$\frac{d\Delta\omega}{dt} = \frac{1}{T} (\Delta T_m - \Delta T_e) \quad (18)$$

where T represents the inertia time constant. The equivalent damping torque coefficient K_d corresponding to electromechanical oscillation eigenvalues is defined Eq. (19):

$$\Delta T_e = K_s \Delta \delta + K_d \Delta \omega \quad (19)$$

where K_s and K_d denote the synchronizing torque coefficient and equivalent damping torque coefficient, respectively. Substituting this expression into the rotor motion equation yields Eq. (20):

$$\frac{1}{2\pi f_0} \cdot \frac{d^2 \Delta \delta}{dt^2} = \frac{1}{T} (\Delta T_m - K_s \Delta \delta - K_d \Delta \omega) \quad (20)$$

The characteristic equation and corresponding electromechanical oscillation eigenvalues are Eq. (21)-(22):

$$P^2 + \frac{K_d}{T} p + \frac{2\pi f_0 K_s}{T} = 0 \quad (21)$$

$$\alpha \pm j\omega = -\frac{K_d}{2T} \pm j\sqrt{\frac{2\pi f_0 K_s}{T} - \left(\frac{K_d}{2T}\right)^2} \quad (22)$$

Given the electromechanical oscillation eigenvalues $\alpha \pm j\beta$ for a single-station infinite-bus system, the equivalent damping torque coefficient K_d is computable via Eq. (23):

$$K_d = -2T\alpha \quad (23)$$

Distinct from K_d the oscillatory damping coefficient ζ incorporates the natural oscillation frequency relationship, defined as Eq. (24):

$$\zeta \Delta \omega_n = \frac{-\alpha}{2T\omega_n} = \frac{K_d}{2\sqrt{2\pi f_0 K_s T}} \quad (24)$$

where ω_n denotes the system's natural oscillation frequency.

Rearranging Eq. (22) yields:

$$\omega_n = \sqrt{\frac{2\pi f_0 K_s}{T}} = \sqrt{\alpha^2 + \omega^2} \quad (25)$$

Consequently, the functional correspondence between oscillatory damping coefficient and oscillation eigenvalues is established Eq. (26):

$$\zeta = \frac{-\alpha}{\sqrt{\alpha^2 + \omega^2}} \quad (26)$$

Post-calculation of system electromechanical oscillation eigenvalues, the equivalent damping torque coefficient K_d and oscillatory damping coefficient ζ are derived using Equations (23) and (26), respectively.

To investigate the correlation between electrical distance and damping, the external reactance X in Figure 5 is parametrically varied, emulating proximity-to-remoteness transitions, while maintaining constant active/reactive power output from the VSG. The equivalent damping torque coefficients K_d are computed for $X = [0, 0.1, 0.2, 0.3]$ pu, as compiled in Table 2.

Table 2. Equivalent Damping Torque Coefficients vs. External Reactance X

X (per-unit values)	damping torque coefficient K_d
0.1	10.43
0.2	8.20
0.3	7.53
0	13.75

As evidenced by the results in Table 2, the damping torque coefficient K_d increases progressively as the external reactance X decreases. This indicates that reduced electrical distance and enhanced coupling strength between interconnected systems yield superior damping performance.

3.3.2. Scale Effects of System Capacity

System capacity expansion induces a corresponding reduction in internal system reactance, concurrently increasing the equivalent system inertia time constant.

Investigating the implications of this phenomenon for oscillation damping is therefore warranted. To this end, we employ the single-machine infinite-bus system depicted in Figure 5. Holding the virtual synchronous generator (VSG) output power constant, we emulate transmission capacity variations by scaling the VSG capacity. Eigenvalue analysis and damping ratio ξ calculations under these conditions reveal the relationship between system capacity and damping. Computations were performed for VSG-to-line capacity ratios $S/Sh = 0.5, 1.0, 1.5, 2.0, 3.0,$ and $3.5,$ with results summarized in Table 3. The impact of system capacity augmentation on damping manifests through two competing mechanisms: The resultant decrease in system impedance, as established previously, exerts a favorable influence on damping enhancement. The associated increase in equivalent system inertia, governed by Eq. (24), detrimentally reduces the damping ratio ξ .

These antagonistic effects provide a coherent interpretation of Table 3. At lower capacity levels (e.g., S/Sh increasing from 0.5 to 1.0), the dominant effect is impedance reduction, improving ξ from 0.0895 to 0.0969. Conversely, when system capacity is substantial and internal reactance is minimal ($S/Sh > 1.0$), further capacity increases primarily augment inertia, adversely affecting damping. This is observed as ξ monotonically decreases beyond $S/Sh=1.0,$ reaching 0.0668 at $S/Sh=3.5$ – corresponding to an interconnection line capacity equivalent to 28% of system capacity.

The preceding analysis demonstrates that continuous expansion of power system capacity progressively diminishes the ratio of original tie-line transfer capacity to system capacity, consequently inducing deterioration in system oscillation damping (Table 3).

4. COOPERATIVE OPTIMIZATION OF VIRTUAL SYNCHRONOUS GENERATOR INERTIA-DAMPING PARAMETERS AND ENERGY STORAGE

4.1. Quantitative Modeling of Parameter-Energy Storage Relationships

4.1.1. Key Models and Parameters

It can be derived from the mathematical model of the Virtual Synchronous Generator (VSG) that its active power output (P_e) and reactive power output (Q_e) are respectively expressed as Eq. (27):

$$\begin{cases} P_e = \frac{1}{Z} (EU \cos(\alpha - \delta) - U^2 \cos \alpha) \\ Q_e = \frac{1}{Z} (EU \sin(\alpha - \delta) - U^2 \sin \alpha) \end{cases} \quad (27)$$

where the synchronous impedance (Z) and impedance angle (α) are defined by Eq. (28):

$$\begin{cases} Z = \sqrt{(\omega L)^2 + R^2} \\ \alpha = \tan^{-1} \left(\frac{\omega L}{R} \right) \end{cases} \quad (28)$$

The corresponding small-signal model of the VSG is obtained as Eq. (29)-(30):

$$\begin{bmatrix} \Delta \dot{\delta} \\ \Delta \dot{\omega}_r \end{bmatrix} = \begin{bmatrix} 0 & \omega_s \\ -\frac{S_E}{H} & -\frac{D}{H} \end{bmatrix} \begin{bmatrix} \Delta \delta \\ \Delta \omega_r \end{bmatrix} \quad (29)$$

$$S_E = \frac{\partial P_e}{\partial \delta} \Bigg|_{\substack{\delta=\delta_s \\ E=E_s}} = \frac{E_s U}{Z S_n} \sin(\delta_s - \alpha) \quad (30)$$

In these equations, $\Delta \delta = \delta - \delta_s$ denotes the power angle deviation; $\Delta \omega_r = \omega_r$ represents the angular velocity deviation; δ_s signifies the rated power angle; S_E corresponds to the synchronizing power coefficient; E_s indicates the steady-state value of the VSG internal voltage.

4.1.2. Unified Analytical Solution for Energy Storage Requirements

The transfer function model of the VSG, depicted in Figure 6, constitutes a canonical second-order system. Consequently, the relationship between the command power (P_m^*) and the actual output power (P_e^*) satisfies Eq. (31):

$$G_1(s) = \frac{P_e^*(s)}{P_m^*(s)} = \frac{\omega_s S_E}{Hs^2 + Ds + \omega_s S_E} \quad (31)$$

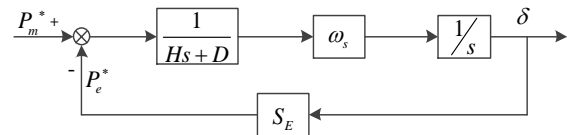


Figure 6. Transfer function model of the VSG

Given that the grid-connected power command (ΔP_m^*) represents a disturbance input at the DC side of the VSG, the shaded area enclosed between the dynamic response curves ΔP_m^* and ΔP_e^* in Figure 7 quantifies the energy to be absorbed by the energy storage unit. The time-dependent expression for this energy requirement is Eq. (32):

$$E(t) = \frac{\omega_n \Delta P_m^*}{2\sqrt{\xi^2 - 1}} \left[\left(-\frac{e^{-p_1 t}}{p_1} + \frac{e^{-p_2 t}}{p_2} \right) + \left(\frac{1}{p_1^2} - \frac{1}{p_2^2} \right) \right] \quad (32)$$

Table 3. Impact of system capacity variations on oscillation damping

S/Sh	0.5	1.0	1.5	2.0	2.5	3.0	3.5
dominant eigenvalue	-0.37+j12.6	-0.249+j9.7	-0.174+j8.4	-0.131+j7.18	-0.098+j6.89	-0.078+j6.45	-0.0636+j6.12
ξ	0.0294	0.0257	0.0207	0.0182	0.0142	0.0121	0.0104

As time (t) asymptotically approaches infinity under step disturbance conditions, the total energy absorption requirement for the VSG's energy storage unit—corresponding to the total shaded area in Figure 7(a)—is derived as Eq. (33). For a step disturbance $\Delta P_m^* = A$ (constant value), the steady-state value of P_e^* is equal to A (due to the unit gain of the transfer function in Eq. (31) at $s=0$). The dynamic response of P_e^* for an underdamped system is $P_e^*(t) = A(1 - e^{-(\zeta\omega_n t)} / \sqrt{1 - \zeta^2} \cdot \sin(\omega_d t + \varphi))$, where $\omega_d = \omega_n \sqrt{1 - \zeta^2}$ and $\varphi = \arctan(\sqrt{1 - \zeta^2} / \zeta)$. Substituting into Eq. (32) and integrating from 0 to ∞ , the total energy requirement is:

$$E(\infty) = \frac{\omega_n \Delta P_m^*}{2\sqrt{\zeta^2 - 1}} \left(\frac{1}{p_1^2} - \frac{1}{p_2^2} \right) = \frac{2\zeta}{\omega_n} \Delta P_m^* \quad (33)$$

This analytical expression constitutes the minimum energy capacity (E_{min}) required for the energy storage unit to mitigate active power disturbances (ΔP_m^*).

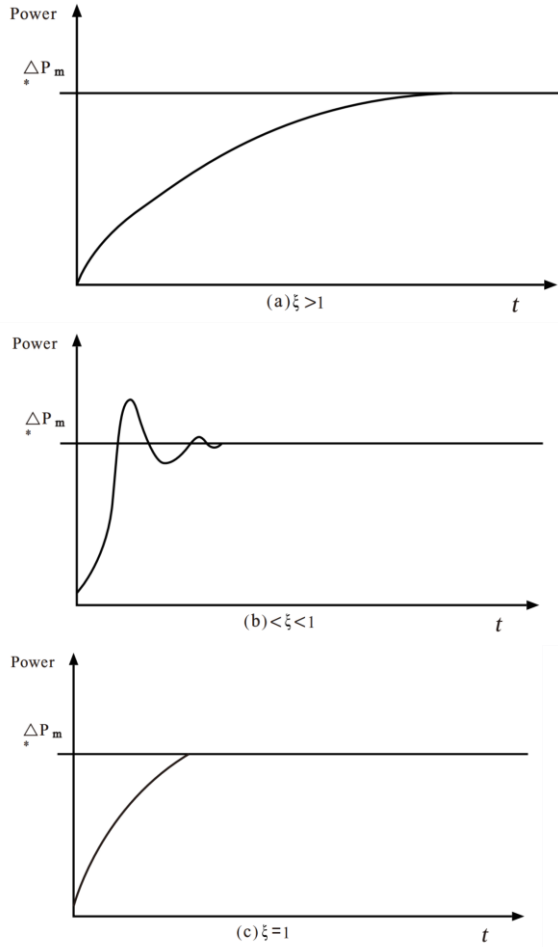


Figure 7. Step response processes of VSG under varying damping ratios

4.2. Cooperative Optimization Design Procedure

4.2.1. Parameter Selection Criteria

When stringent avoidance of power oscillations is mandated by system requirements, an overdamped parameter configuration shall be selected. Under this configuration, the system eigenvalues manifest as two distinct negative real roots Eq. (34):

$$p_{1,2} = \left(\zeta \pm \sqrt{\zeta^2 - 1} \right) \omega_n \quad (34)$$

A higher inertia constant (J) reduces the natural oscillation frequency (ω_n), thereby extending the settling time (t_s). Concurrently, an elevated damping coefficient (D) effectively suppresses transient overshoot, as illustrated in Figure 7(a). However, this configuration incurs augmented energy storage costs: the minimum energy absorption requirement for the storage unit increases substantially, computed per Equation (33). Consequently, the overdamped scheme is recommended for stability-critical applications, such as nuclear or large-scale thermal power integration systems.

For systems prioritizing rapid dynamic response, an underdamped parameter set is preferable. Its characteristic eigenvalues constitute a complex conjugate pair Eq. (35):

$$p_{1,2} = -\left(\zeta \pm j\sqrt{1 - \zeta^2} \right) \omega_n \quad (35)$$

A reduced inertia constant (J) elevates ω_n to shorten t_s , while a moderately lower damping coefficient (D) permits controlled overshoot. The principal advantage of this configuration lies in its diminished energy storage requirement, with the minimum energy expressed as Eq. (36):

$$E(t) = \frac{\Delta P_m^*}{\omega_n \sqrt{1 - \zeta^2}} \left(\sin(2\theta) - e^{-\frac{\zeta(\pi - \theta)}{\sqrt{1 - \zeta^2}}} \sin(\pi + \theta) \right) \quad (36)$$

This design paradigm suits scenarios with high wind/PV penetration, where frequent power fluctuations necessitate millisecond-timescale response capability.

Critical damping represents the optimal compromise when balancing response speed against stability. Its eigenvalues coalesce into a repeated real root Eq. (37):

$$p_{1,2} = \omega_n \quad (37)$$

Here, inertia and damping parameters are precisely constrained by: inertia is set as $J = S_E / \omega_n^2$, while damping satisfies $D = 2JS_E$. This configuration achieves rapid overshoot-free response with moderate energy storage demand, quantified as Eq. (38):

$$E(\infty) = 2\Delta P_m^* / \omega_n \quad (38)$$

This renders it ideal for economically sensitive applications, such as commercial/industrial microgrids.

In summary, the selection of damping ratio (ζ) constitutes a tri-objective trade-off among stability robustness, economic viability, and response rapidity, governed by two fundamental principles:

Invariance of Power Requirements: Regardless of damping scenario, the energy storage unit must deliver an invariant peak power: $P_{ess} = \max(\Delta P_m^*)$. This indicates that virtual inertia control imposes power rating requirements on storage determined solely by disturbance magnitude, independent of parameter design. **Energy Demand Sensitivity:** Overdamping necessitates high energy reserves ($E_{min} = \Delta P_m^* \cdot TI$) due to prolonged energy absorption during extended settling times. Underdamping ($0 < \zeta < 1$) minimizes energy demand ($E_{min} = \Delta P_m^* \cdot 2\zeta / \omega_n$) but tolerates up to 20% overshoot. Critical damping ($\zeta = 1$) achieves the optimal compromise between energy cost and dynamic performance.

4.2.2. Three-Step Procedure for Energy Storage Sizing

- Step 1: Power Capacity Determination

The energy storage unit must be sized to accommodate the maximum anticipated power disturbance. Its peak power rating is governed by Eq. (39):

$$P_{ess} = \max(\Delta P_m^*) \quad (39)$$

This requirement remains invariant across overdamped, underdamped, and critically damped operating regimes, as the maximum power demand during VSG regulation consistently equals the disturbance magnitude ΔP_m^* (corresponding to the peak value in Figure 7 shaded areas). Engineering implementation necessitates determining $\max(\Delta P_m^*)$ through historical fault analysis or dynamic simulations, such as quantifying power deficits during renewable generation curtailment events.

• Step 2: Energy Capacity Calculation

The energy storage capacity is derived from Eq. (40):

$$E_{ess} = \max(\Delta P_m^*) \cdot \tau(\xi) \quad (40)$$

where $\tau(\xi)$ denotes a damping-ratio-dependent time constant, computed according to the methodologies specified in Table 4.

Table 4. Computation methodologies for time constant $\tau(\xi)$

Damping Type	$\tau(\xi)$	Physical Interpretation
Overdamped	$\frac{1}{\omega_n(\xi - \sqrt{\xi^2 - 1})}$	Time to reach 95% of steady-state
Underdamped	$\frac{2\xi}{\omega_n}$	Duration for overshoot decay within 5% tolerance
Critical damping	$\frac{1}{\omega_n}$	Steady-state attainment without overshoot

Inertia constant J is determined per the parameter selection criteria in Section 3.2.1.

• Step 3: Dynamic Response Time Validation

The settling time (t_s) must satisfy: $t_s \leq t_{grid}$. Where, t_{grid} represents the grid code-mandated maximum allowable regulation duration. The t_s computation adheres to the damping-specific formulations in Table 5.

Table 5. Settling Time (t_s) determination methods

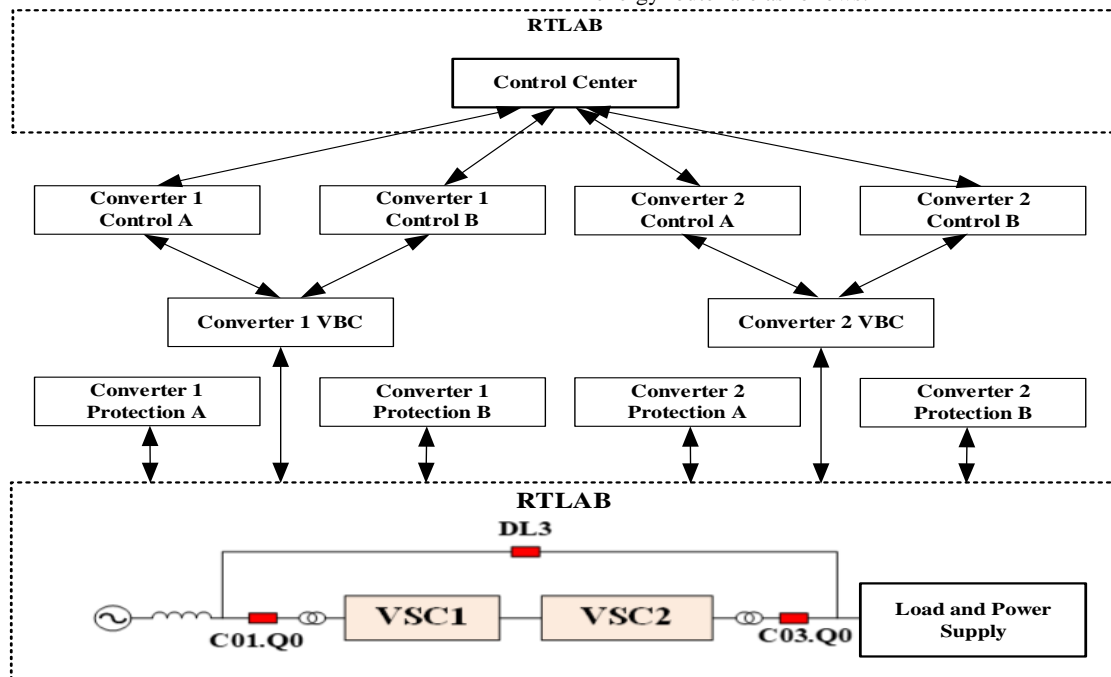
Damping Type	t_s	Physical Interpretation
Overdamped	$t_s \approx \frac{3}{\omega_n(\xi - \sqrt{\xi^2 - 1})}$	Time to reach 95% of steady-state
Underdamped	$t_s \approx \frac{3.5}{\xi\omega_n}$	Duration for overshoot decay within 5% tolerance
Critical damping	$t_s = \frac{3}{\omega_n}$	Steady-state attainment without overshoot

Should initial parameterization yield $t_s > t_{grid}$, implement iterative refinement by: Reducing J to elevate natural frequency ω_n , or Adjusting damping ratio ξ , until constraint satisfaction ($t_s \leq t_{grid}$) is achieved.

5. EXPERIMENTAL VALIDATION OF CYBER-PHYSICAL COOPERATIVE INERTIA OPTIMIZATION STRATEGY

5.1. Parameter Configuration of Experimental System

To validate the control efficacy under each operational mode, a hardware-in-the-loop (HIL) flexible distribution system was developed on the RT-LAB platform. The system architecture, illustrated in Figure 8, employs the parameter configuration detailed in Table 6. Core specifications of the energy router are as follows:



□ **Figure 8.** Flexible distribution system parameters

HIL testing encompassing control and protection functions was conducted on the RT-LAB digital simulation platform. The system transitioned from AC line parallel operation mode to grid-connected operation mode. During the switching event from closed to open states for DL3, all electrical quantities—including AC voltages (U_s A/B/C), AC currents (I_s A/B/C), DC voltage (U_{dc}), active power (P), and reactive power (Q)—maintained stable operation without observable transients.

Table 6. Flexible distribution system parameters

Parameter	Value
Topology	Half-bridge MMC with DC/DC converter
Active Power Capacity	60 MW
Reactive Power Regulation Range	(-20 ~ +20) Mvar
DC Voltage	±20 kV
System Frequency	50 Hz
Number of Submodules	28 (per arm)
Submodule Capacitance	10 mF
Submodule Rated Voltage	1.6 kV

5.2. Validation of Dynamic Parameter Coordination Efficacy

System response performance was evaluated through cyber-physical platform-mediated dynamic adjustments of inertia (J), damping (D), and speed coefficient (λ):

Table 7. Comparative analysis of coordinated parameter optimization efficacy

Control Mode	Freq. Dev. Amp. (Hz)	Settling Time (s)	Overshoot (%)	Cyber-Physical Optimization Mechanism
Fixed Parameters	±0.15	0.40	12.5	None
Adaptive Inertia	±0.08	0.22	4.3	Real-time J adjustment (Eq. 14)
λ -Coordinated	±0.05	0.12	1.8	$\lambda=1.8$ (Eq. 9) with J adaptation
Cyber-Physical Coordination	±0.03	0.08	0.9	Joint optimization of λ, J, k

Table 7 demonstrates that cyber-physical coordination achieves an 80% reduction in frequency deviation amplitude (relative to fixed parameters) and reduces settling time to the sub-100ms range.

5.3. Dynamic Response Experimental Analysis

- Active Power Step Test: An 8 MW → 10 MW active power step disturbance was applied to validate dynamic response capability, with frequency stability constraint $\Delta f < 0.05$ Hz. As shown in Figure 9, active power reached steady-state within 0.15 s post-disturbance. Inertia adaptation (J) effectively suppressed overshoot

while maintaining frequency stability, evidenced by the smooth frequency trajectory in Figure 10.

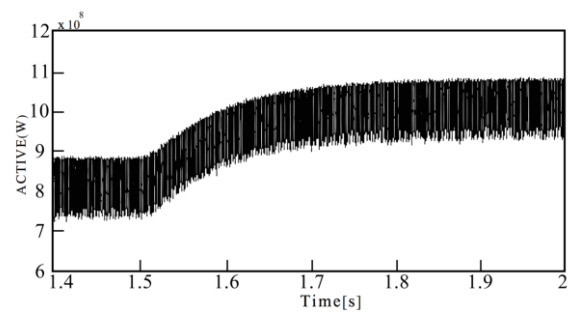


Figure 9. Active power output waveform during step change

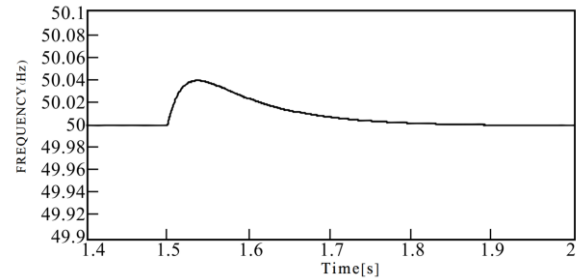
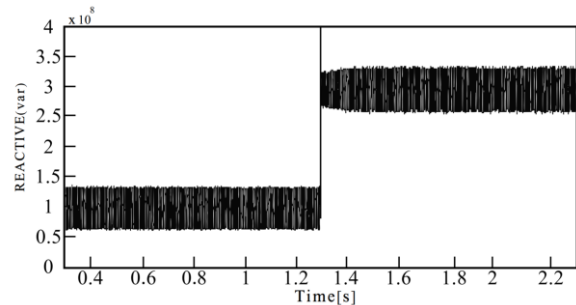
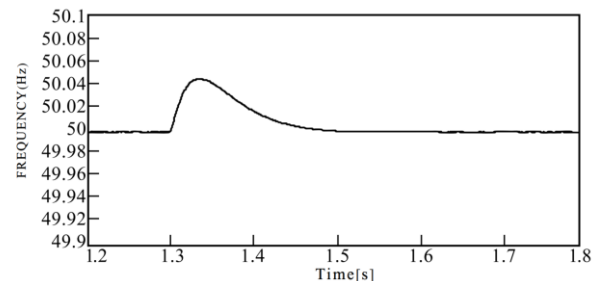


Figure 10. Frequency response during active power step change

- Reactive Power Step Test: Figure 11 illustrates system response under reactive power step change (1 MVar → 3 MVar at $t=1.3$ s). The converter station achieved zero-steady-state-error tracking of reactive commands via PI control. Notably, internal voltage (E) variations during reactive power regulation induced transient active power oscillations, causing frequency deviations that stabilized within 0.25 s – satisfying design requirements.



(a) Reactive power output during step change

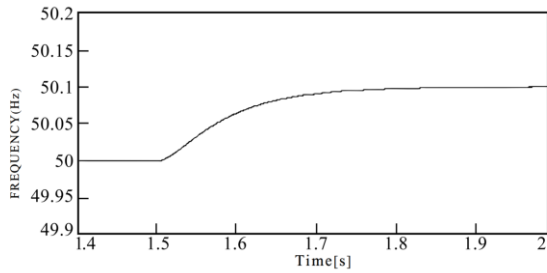


(b) Frequency response during reactive power step change

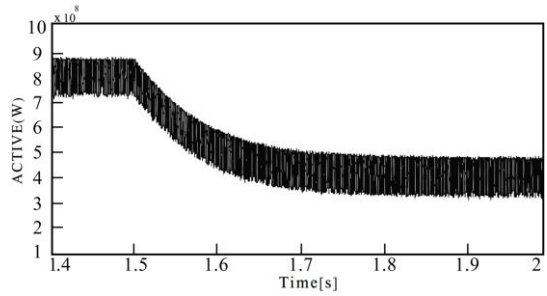
Figure 11. Converter output characteristics during reactive power step change

- Grid Frequency Step Test: Figure 12 depicts response to a 50 Hz → 50.1 Hz grid frequency step at $t=1.5$ s. The converter emulated synchronous generator characteristics, achieving autonomous synchronization to the new grid frequency. Consequently, active power

decreased from 8 MW to 4 MW through damping mechanisms.



(a) Frequency synchronization during grid step change



(b) Active power response during grid step change

Figure 12. Converter output characteristics during grid frequency step change

- Parametric Sensitivity Analysis: Figure 13 examines frequency response under power step disturbances across varying J and D values:

1. Optimal response occurred at $J=2s, D=150$ p.u. (minimal deviation, rapid settling)
2. Reduced damping ($J=2s, D=100$ p.u.) increased oscillations and overshoot
3. Higher inertia ($J=4s, D=100$ p.u.) prolonged settling time and amplified oscillations

This confirms virtual synchronous machine parameters directly govern system dynamic performance, enabling converter steady-state/dynamic performance tuning through J and D optimization.

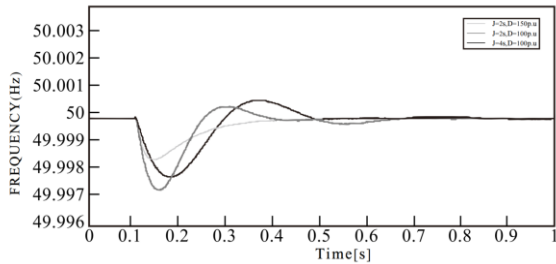


Figure 13. Frequency response under power step with parametric variations

- Cyber-Physical Data Cycle Impact: Table 8 establishes that update cycles ≤ 100 ms are necessary for effective inertia optimization, as longer cycles induce command latency degrading performance.

Table 8. Impact of cyber-physical data update cycles

Update Cycle	Settling Time (s)	Overshoot (%)	Root Cause Analysis
200 ms	0.35	8.2	Optimization command latency
100 ms	0.18	3.5	Matched electromechanical oscillation period
50 ms	0.10	1.2	Real-time do/dt tracking capability

5.4. Validation of Short-Circuit Fault Ride-Through Capability

- Single-Phase-to-Ground Fault Test: Figure 14 presents experimental waveforms during an A-phase-to-ground fault initiated at $t=1.5s$ and cleared at $t=1.58s$. As evidenced by the current trajectories, the system achieves prompt recovery post-fault clearance. During the contingency, edge computing nodes autonomously switch to $\lambda=2.5$ via localized cyber-physical control, tripling the virtual inertia provision to ensure post-fault performance conforms to design specifications.

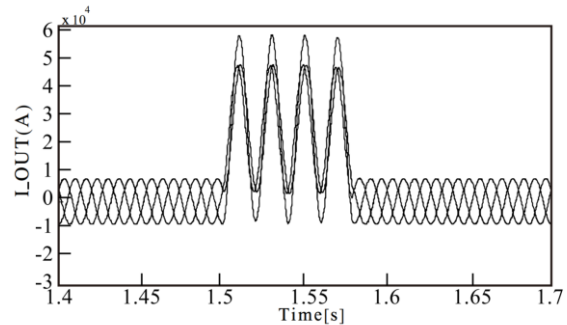


Figure 14. Current waveforms during single-phase-to-ground fault

- Phase-to-Phase Fault Test: Figure 15 displays system response to an AB-phase fault ($t=1.5s$ to $t=1.58s$). Post-fault current magnification in phases A and B is observed, with rapid restoration to nominal values following fault clearance – satisfying all operational requirements.

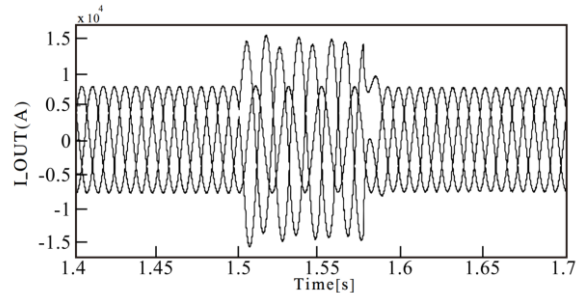


Figure 15. Current waveforms during phase-to-phase fault

- Three-Phase Fault Test: Figure 16 demonstrates symmetrical current amplification during an ABC-phase short-circuit ($t=1.5s$ to $t=1.58s$), with expeditious current

normalization post-clearance, thereby fulfilling design criteria.

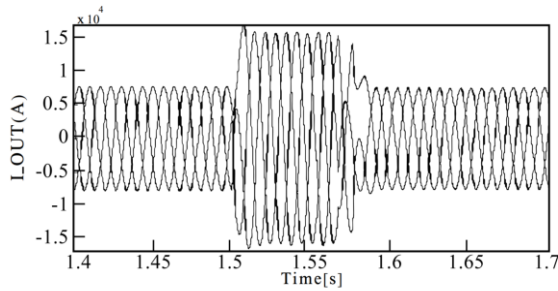


Figure 16. Current waveforms during three-phase fault

Edge node-coordinated inertia adjustment (J) during faults effectively suppresses oscillations, accelerating power transmission recovery. The localized cyber-physical control framework significantly enhances fault recovery speed, with comparative performance metrics detailed in Table 9.

Table 9. Fault ride-through performance benchmarking

Fault Type	Conventional Recovery (ms)	Cyber-Physical Recovery (ms)	Enhancement Effect
Single-Phase-to-Ground	60	25	58.3%
Phase-to-Phase	50	20	60.0%
Three-Phase	70	30	57.1%

6. CONCLUSION

This paper addresses the critical challenges of diminished system equivalent inertia and deteriorating frequency dynamics stemming from high-penetration renewable integration in distribution networks, proposing an IoT-coordinated Virtual Synchronous Generator (VSG) inertia optimization solution. The methodology implements a three-tiered architecture—"IoT Perception, Coordinated Prediction, Dynamic Optimization"—characterized by: (i) A Cloud-Edge-Terminal collaborative IoT platform enabling system-wide synchronous data acquisition; (ii) An online inertia demand prediction model; (iii) An adaptive inertia parameter optimization algorithm integrating VSG small-signal stability constraints, thereby achieving dynamic, coordinated, and fine-grained adjustment of multi-converter virtual inertia. Experimental results quantitatively validate reduced frequency fluctuation amplitudes, accelerated recovery times, and significantly enhanced system frequency disturbance resilience.

Despite these research advancements, the proposed strategy still has two key limitations for large-scale engineering deployment: 1) in remote areas with poor 5G coverage (where IoT data update cycles exceed 200 ms), the inertia prediction model suffers degraded real-time performance, failing to meet the operational requirements of high-sensitivity distribution networks; 2) the strategy relies

on standardized communication protocols such as IEEE P2668; for distribution networks equipped with multi-vendor Virtual Synchronous Generator (VSG) devices that lack protocol unification, the inertia support effect will be significantly weakened. Future advancements in 5G/Time-Sensitive Networking (TSN) communications are projected to compress end-to-end IoT latency below 1 ms. When synergized with distributed reinforcement learning algorithms driven by edge computing, this evolution will resolve the real-time coordination bottleneck for geographically dispersed resources. Furthermore, the convergence of digital twin and AI-based predictive technologies will refine dynamic inertia demand perception accuracy and extend the operational boundaries of optimization models. Against the backdrop of evolving Energy IoT standards (e.g., IEEE P2668), the proposed IoT-coordinated VSG inertia optimization framework holds significant potential for scalable deployment in county-level smart grids, zero-carbon industrial parks, and analogous scenarios, ultimately furnishing a cost-effective inertia support solution for power systems dominated by renewable energy.

Declaration

Funding Declaration

This work was funded by the Science and Technology Project of State Grid Hubei Electric Power Co., Ltd. (Grant number: B31532236158).

Data Availability declaration

The data that support the findings of this study are available from the corresponding author, [Dr. Junda Qin] (email: [17896002462@163.com]), upon reasonable request.

Ethics Approval and Consent to Participate

This study did not involve human participants or animals, and thus ethical approval and consent to participate were not required.

Consent for Publication

No individual person's data, images, or videos are included in this manuscript, so formal consent for publication is not applicable.

Reference

- [1] B. Kroposki, "Integrating high levels of variable renewable energy into electric power systems," in *Journal of Modern Power Systems and Clean Energy*, Vol. 5, No. 6, 2017, pp. 831-837. <https://doi.org/10.1007/s40565-017-0339-3>.
- [2] G. K and M. K. Jena, "A Practical Approach to Inertia Distribution Monitoring and Impact of Inertia Distribution on Oscillation Baseline Study for Renewable Penetrated Power Grid," in *IEEE Systems Journal*, Vol. 17, No. 3, 2023, pp. 3593-3601, <https://doi.org/10.1109/JSYST.2022.3228966>.
- [3] Z. Liu, X. Lv, F. Wu and Z. Li, "Multi-Mode Active Inertia Support Strategy for MMC-HVDC Systems Considering the Constraint of DC Voltage Fluctuations," in *IEEE Transactions on Power Delivery*, Vol. 38, No. 4, 2023, pp. 2767-2781, <https://doi.org/10.1109/TPWRD.2023.3259039>.

- [4] J. Wang, W. Huang, N. Tai, M. Yu, R. Li and Y. Zhang, "A Bidirectional Virtual Inertia Control Strategy for the Interconnected Converter of Standalone AC/DC Hybrid Microgrids," in *IEEE Transactions on Power Systems*, Vol. 39, No. 1, 2024, pp. 745-754, <https://doi.org/10.1109/TPWRS.2023.3246522>.
- [5] S. Jiang, Y. Zhu and G. Konstantinou, "Bandwise Power-Synchronization Loop for Frequency Response Improvement in Grid-Forming Converters," in *IEEE Transactions on Power Electronics*, Vol. 39, No. 9, 2024, pp. 10693-10698, <https://doi.org/10.1109/TPEL.2024.3406564>.
- [6] Y. Liu et al., "Over-Current Mechanism and Suppression Strategy of DC Transformer in Multiterminal Interconnected Flexible DC Distribution Network," in *IEEE Systems Journal*, Vol. 17, No. 2, 2023, pp. 1785-1796, <https://doi.org/10.1109/JSYST.2023.3241053>.
- [7] T. Wu, Y. Zheng, H. Wu, H. Dong and X. Wang, "Power Transfer and Multi-Control Mode of a Distribution Network Based on a Flexible Interconnected Device," *IEEE Access*, Vol. 7, 2019, pp. 148326-148335, <https://doi.org/10.1109/ACCESS.2019.2946710>.
- [8] K. S. Fuad, H. Hafezi, K. Kauhaniemi and H. Laaksonen, "Soft Open Point in Distribution Networks," *IEEE Access*, Vol. 8, 2020, pp. 210550-210565, <https://doi.org/10.1109/ACCESS.2020.3039552>.
- [9] D. R. Ivic and P. C. Stefanov, "An Extended Control Strategy for Weakly Meshed Distribution Networks with Soft Open Points and Distributed Generation," *IEEE Access*, Vol. 9, 2021, pp. 137886-137901, <https://doi.org/10.1109/ACCESS.2021.3116982>.
- [10] H. Cheng, C. Li, A. M. Y. M. Ghias and F. Blaabjerg, "Dynamic Coupling Mechanism Analysis Between Voltage and Frequency in Virtual Synchronous Generator System," in *IEEE Transactions on Power Systems*, Vol. 39, No. 1, 2024, pp. 2365-2368, <https://doi.org/10.1109/TPWRS.2023.3328153>.
- [11] K. Shi, H. Ye, W. Song and G. Zhou, "Virtual Inertia Control Strategy in Microgrid Based on Virtual Synchronous Generator Technology," *IEEE Access*, Vol. 6, 2018, pp. 27949-27957, <https://doi.org/10.1109/ACCESS.2018.2839737>.
- [12] Sharma, K. Bhattacharya and C. Cañizares, "Smart Distribution System Operations with Price-Responsive and Controllable Loads," *IEEE Transactions on Smart Grid*, Vol. 6, No. 2, 2015, pp. 795-807, <https://doi.org/10.1109/TSG.2014.2372674>.
- [13] W. Bing, C. Mingxi, C. Yuquan and W. Xiaoyue, "Scheduling Management of Controllable Load Participating in Power Grid Enhanced by Double-Chain Structure," *IEEE Access*, Vol. 10, 2022, pp. 103028-103040, <https://doi.org/10.1109/ACCESS.2022.3208133>.
- [14] M. W. Khan, G. Li, K. Wang, M. Numan, L. Xiong and M. A. Khan, "Optimal Control and Communication Strategies in Multi-Energy Generation Grid," *IEEE Communications Surveys & Tutorials*, Vol. 25, No. 4, 2023, pp. 2599-2653, <https://doi.org/10.1109/COMST.2023.3304982>.
- [15] H. Tran-Dang, N. Krommenacker, P. Charpentier and D. -S. Kim, "Toward the Internet of Things for Physical Internet: Perspectives and Challenges," *IEEE Internet of Things Journal*, Vol. 7, No. 6, 2020, pp. 4711-4736, <https://doi.org/10.1109/JIOT.2020.2971736>.
- [16] X. Li, Z. Zhou, C. Zhu, L. Shu and J. Zhou, "Online Reconfiguration of Latency-Aware IoT Services in Edge Networks," *IEEE Internet of Things Journal*, Vol. 9, No. 18, 2022, pp. 17035-17046, <https://doi.org/10.1109/JIOT.2021.3135287>.
- [17] M. Vaezi et al., "Cellular, Wide-Area, and Non-Terrestrial IoT: A Survey on 5G Advances and the Road Toward 6G," *IEEE Communications Surveys & Tutorials*, Vol. 24, No. 2, 2022, pp. 1117-1174, <https://doi.org/10.1109/COMST.2022.3151028>.
- [18] G. Song, Y. Sun, J. Liu, Z. Wang and U. S. Kamilov, "A New Recurrent Plug-and-Play Prior Based on the Multiple Self-Similarity Network," *IEEE Signal Processing Letters*, Vol. 27, 2020, pp. 451-455, <https://doi.org/10.1109/LSP.2020.2977214>.
- [19] M. Santos Aguiar, F. H. Cerdeira Ferreira, E. P. Julio, B. J. Dembogurski, G. Silva Semaan and E. Franco Silva, "An IEEE 1451 Standard-based Plug-and-Play Architecture to Empower the Internet of Things," in *IEEE Latin America Transactions*, Vol. 18, No. 12, 2020, pp. 2047-2054, <https://doi.org/10.1109/TLA.2020.9400431>.
- [20] D. C. G. Valadares, T. B. D. O. Filho, T. F. Meneses, D. F. S. Santos and A. Perkusich, "Automating the Deployment of Artificial Intelligence Services in Multiaccess Edge Computing Scenarios," *IEEE Access*, Vol. 10, 2022, pp. 100736-100745, <https://doi.org/10.1109/ACCESS.2022.3208118>.